nature communications

Article

https://doi.org/10.1038/s41467-024-55675-z

Grand canyons on the Moon

Received: 30 May 2024

Accepted: 20 December 2024

Published online: 04 February 2025

Check for updates

David A. Kring [1], Danielle P. Kallenborn [1,2] & Gareth S. Collins [2]

High energy streams of rock ejected from the Schrödinger impact basin carved two canyons in the lunar crust that are comparable in size to the Grand Canyon of North America. Here we use photogeologic mapping of those canyons and related impact ejecta deposits to show the trajectory of the impacting asteroid or comet, which produced an asymmetrical pattern of crater excavation and transport of ejected debris. The flow directions of that ejected debris and the speed of its subsequent impact with the lunar surface are calculated, as is the energy that carved the canyons in less than ten minutes. The study implies that most of the excavated debris was ejected away from the lunar south pole, minimizing the amount of debris that covers the > 4 billion year old units that will be explored by Artemis astronauts.

A global lunar landing site analysis[1] found that the Schrödinger impact basin[2] is the best location for addressing National Research Council science objectives for lunar exploration[3], prompting geologic studies of the basin and analyzes of potential landing sites for human and robotic missions[4–18]. The first robotic mission is scheduled to land in 2026. Schrödinger basin is also the best analog surface expression for Earth's buried Chicxulub impact crater[19], which is linked to the extinction of dinosaurs and most life at the end of the Cretaceous[20–23]. The Schrödinger impact basin is remarkable for streams of rocky debris that it ejected, carving two canyons that are comparable to Earth's Grand Canyon in width and depth. Here we describe those canyons, how they formed, and the implications they have for the trajectory of the impactor.

Results and discussion

Geologic context

The Schrödinger impact basin (Fig. 1) is a peak-ring basin, ~320 km in diameter, ~4.5 km deep, centered at 75°S, 132.5°E (ref. 8, Supplementary Fig. 1), with an estimated age of $3.81^{+0.013}_{-0.014}$ Ga (ref. 24), although some models suggest ~0.15 Ga uncertainty on basins with late Imbrian ages[25]. Schrödinger's ~150 km diameter peak ring, a circular mountain range that rises 1 to 2.5 km above the basin floor, was produced by the collapse of a central uplift[14]. Basalt lava flows and a large pyroclastic vent later erupted on the basin floor and ceased erupting $3.70^{+0.02}_{-0.03}$ Ga (ref. 18). Schrödinger formed in the outer margin of the ~2400 km-diameter South Pole-Aitken (SPA) basin[26], which is the largest and oldest impact basin on the Moon. The rim of the Schrödinger basin is within 300 km of the south pole and within 125 km of the Artemis exploration zone, which is the first destination of Artemis astronauts.

The Schrödinger basin is surrounded by an asymmetrical ejecta blanket (Fig. 1) that has been mapped[27] up to distances of 500 km from the basin rim, although ejecta components not visible from orbit would have been deposited at far greater distances. The basin is also surrounded by several impact ejecta rays (ref. 28; Supplementary Figs. 2 and 3), including Vallis Schrödinger and Vallis Planck (Fig. 1), which are the foci of this work. Such rays are the result of closely-spaced and radially-aligned secondary impact craters that excavated deep canyons in the lunar crust.

Canyon dimensions

Vallis Schrödinger is ~270 km long, ~20 km wide, ~2.7 km deep, and occurs within the limits of the continuous ejecta blanket. The deepest portion of Vallis Planck is ~280 km long, ~27 km wide, and ~3.5 km deep, but a ray of secondary craters extends beyond the continuous ejecta blanket to a length of 860 km. For comparison, the length of the sinuous Grand Canyon is 446 km (277 river miles) between Lees Ferry and Grand Wash Cliffs, which includes the length of Marble Canyon. The deepest point of the Grand Canyon is 1.949 km (6393 ft) below the north rim near Nankoweap Rapids and 1.452 km (4765 ft) below the south rim near Cremation Creek. For illustration purposes (Fig. 2), a transect of Vallis Planck is compared with the Grand Canyon along the Bright Angel Trail, which is a location familiar to most Grand Canyon National Park visitors.

Fifteen secondary craters are discernable along the length of Vallis Schrödinger, with diameters between 10 and 16 km, clearly defined by their eroded but still visible crater rims (Fig. 3, Supplementary Fig. 4). The maximum diameter of secondary craters produced by primary craters ≤ 260 km in diameter is 4% of the primary

[1]Lunar and Planetary Institute, Universities Space Research Association, 3600 Bay Area Blvd., Houston, TX, US. [2]Department of Earth Science and Engineering, Imperial College London, London, UK. e-mail: kring@lpi.usra.edu

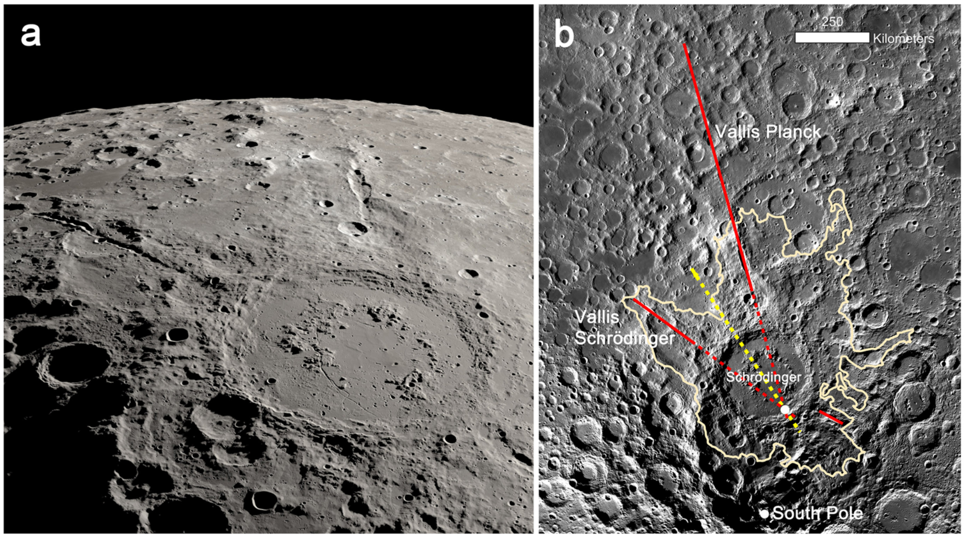

Fig. 1 | Schrödinger impact basin. a Orbital view of the Schrödinger peak-ring impact basin and two radiating canyons carved by impact ejecta. NASA\SVS\Ernest T. Wright. **b** Azimuthal Equidistant Projection of the Moon LRO LROC WAC Global Morphology Mosaic 100 m v3 (100 meters/pixel), centered on the Schrödinger basin, with the continuous ejecta blanket outlined (beige, after ref. 27) and radial secondary crater rays (red). Vallis Schrödinger and Vallis Planck (see Fig. 3 for close-up views) intersect near the southern rim of the basin (white point). The size of the point indicates the uncertainty. The projected bearing of the primary impactor (yellow) runs through the point of intersection and the basin center. A third unnamed feature extends in an uprange direction.

crater's diameter[29], which, if extrapolated to the 320 km diameter Schrödinger basin, implies 13 km. Observed 10–16 km dimensions of secondary craters in Vallis Schrödinger approach and slightly exceed that value.

On the Moon, the depth/diameter (d/D) of fresh primary craters < 15 km in diameter is $0.196^{+0.038}_{-0.027}$ (ref. 30) with those 400 m to 10 km in the polar region is 0.21 (ref. 31). The d/D value of lower-velocity secondary craters is less, ~0.1 for small craters[32]. While no fresh secondary craters produced by basin-size primary craters exist, we infer that the craters along Vallis Schrödinger likely had a d/D value < 0.2 when formed. Measurements after ~3.8 billion years of erosion indicate an average d/D of 0.14 for Vallis Schrödinger and 0.11 for Vallis Planck.

Craters are partly overlapping and superposed by younger craters. Secondary craters are not everywhere preserved along the length of Vallis Planck, which was modified by the collapse of canyon walls as seen in images (Fig. 3) and a topographical transect (Fig. 2). Both canyons suffered erosion, mostly driven by impact gardening of the regolith, seismic slumping, and downslope creep. The upper canyon walls are the steepest portions of the crater rays and have slopes of 27 to 34°, which is the angle of repose for lunar highland material (30°; ref. 33).

Canyon excavation

Velocities of secondary ejecta are 0.95, 0.97, and 1.05 km/s for Vallis Schrödinger assuming ballistic angles of 45, 30, and 20°, respectively (Fig. 4) (see "Methods"). Maximum velocities of ejecta to produce Vallis Planck are larger (1.23 to 1.28 km/s), reflecting longer travel distances. Those velocities are about 50% of the escape velocity from the Moon (2.38 km/s). Flight times of debris producing the 270 km-long main canyon are 4.9 to 15.0 min for Vallis Schrödinger over the entire range of potential ejection angles, with canyon-forming secondary impacts occurring within a 5 min interval. Flight times of debris producing the 280 km-long main canyon are 5.2 to 15.4 min for Vallis Planck over the entire range of potential ejection angles, with canyon-forming secondary impacts occurring within a 5 min interval.

At these ejection speeds, theoretical estimates of mean ejecta fragment sizes range from one-fiftieth to one-twentieth of the primary impactor diameter[34], which was ~25 km for the Schrödinger impact[14]. This implies mean ejecta fragment sizes of 0.5 to 1.25 km diameter at the range of the Schrödinger canyons. This is consistent with our calculated secondary crater projectile diameters for Vallis Planck, which are mostly < 2 km (Fig. 4). On the other hand, the implied projectile diameters for the secondary craters that carved Vallis Schrödinger range from 2.3 to 5.2 km, which are considerably larger than theory would suggest. This suggests that the canyon-carving secondary craters for the more proximal Vallis Schrödinger formed by near simultaneous impact of clusters of ejecta fragments, rather than by impact of individual ejecta fragments. Clusters of secondary craters are commonly observed[35,36] and produce shallow d/D as observed in the Schrödinger rays. Further, those clusters of fragments spread out with radial distance beyond the continuous ejecta blanket[36]. Thus, it is logical that clusters closer to the point of impact (i.e., within the continuous ejecta blanket) would have a smaller spread (be more tightly clustered) and produce simple craters like those observed. In the more distal portions of Vallis Planck, where the areal density of ejecta fragments is lower, the secondary craters are more likely to be formed by individual fragments.

As shown in Fig. 4, the transition in fragment size is abrupt and coincides with the edge of the continuous ejecta blanket. The transition is evident both between the rays and within the Vallis Planck data, where one crater lies within the continuous ejecta. This suggests that the difference in fragment size (or crater size) cannot be attributed to target heterogeneities between the two rays. Either side of the transition, fragment sizes are consistent as a function of distance, which is one of the criteria used to discriminate secondary craters from primary craters[37].

Trajectories and energy

The canyon-forming rays are asymmetrically distributed around the Schrödinger basin and do not converge at the basin center. Rather, the bearings of Vallis Schrödinger and Vallis Planck converge at 78.21947°S, 143.71996°E (Fig. 1). If that convergence is the point of first impact[38], then a line from that point through the basin center suggests a SSE to NNW trajectory (33.5° west of north; Fig. 1) for the impacting asteroid or comet. Thus, rather than a point explosion, like that characterizing small impact events (e.g., Meteor Crater on Earth[39]), the distance between that point of impact and the center of the basin

https://doi.org/10.1038/s41467-024-55675-z

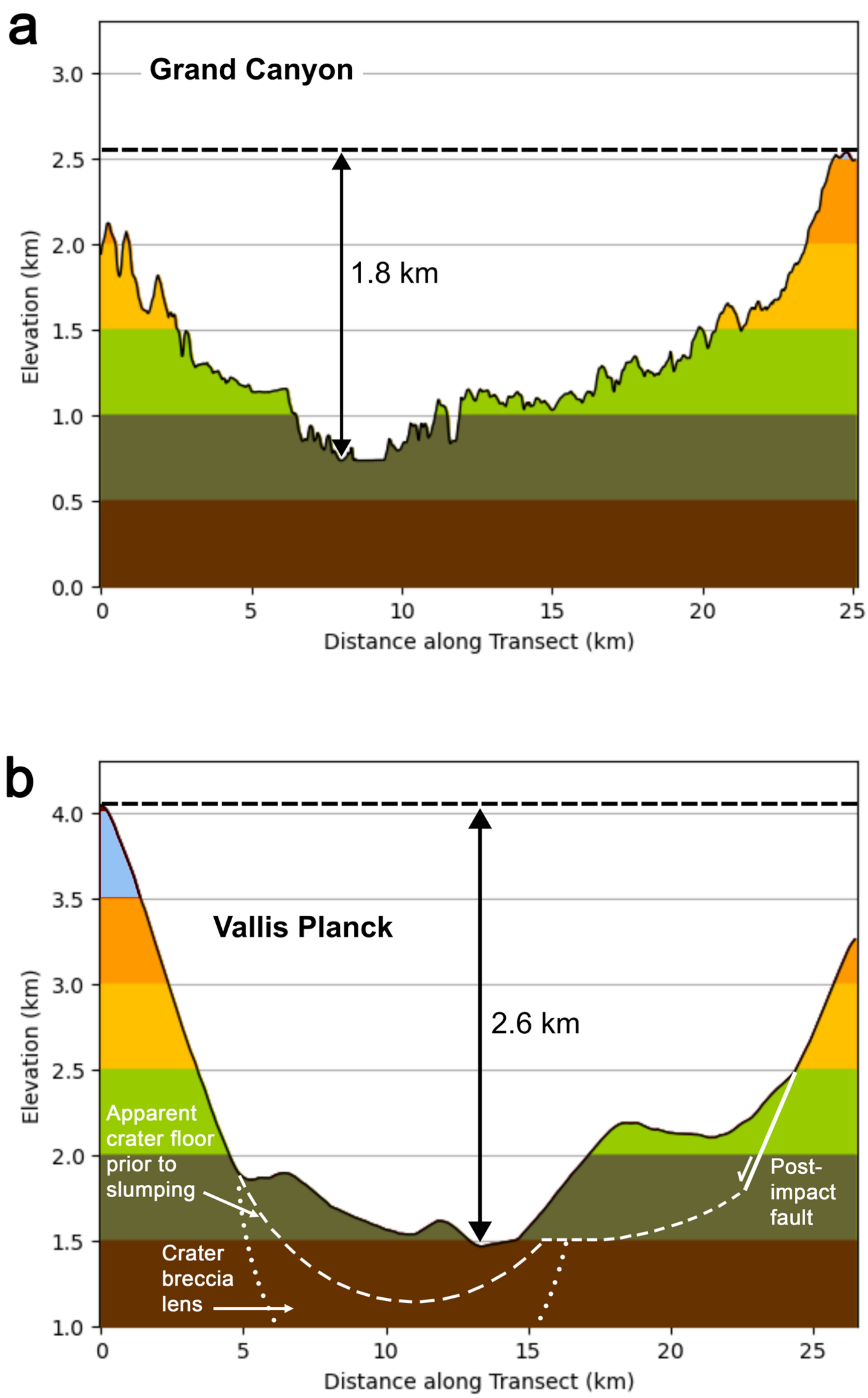

Fig. 2 | Comparison of canyon cross-sections. a Width and depth of the Grand Canyon along the Bright Angel hiking trail from the south to the north rim (annotated in Supplementary Fig. 4). **b** Width and depth of Vallis Planck. The cross-section of Vallis Schrödinger is in Supplementary Fig. 6. Colors show 500 m elevation steps.

implies a distributed impact zone. That distributed impact zone is reflected in the bearings of other, smaller rays of ejecta (Supplementary Fig. 3) that were produced by material ejected as the projectile penetrated deeper into the target and it moved towards the basin center[40]. A distributed impact zone may imply a relatively low primary impact angle[38,41,42]. Likewise, it may imply relatively low angles for secondary ejecta, ranging from 20 to 45° (ref. 42). Because the secondary craters are circular, the ballistic flight angles are probably in the upper end of that range (i.e., 30 to 45°; ref. 43).

Alternatively, the rays may be lateral sprays of ejecta[44] (i.e., part of a butterfly pattern) from an impact with a trajectory of 22.3° east of north, as implied by the largest swath of continuous ejecta (Fig. 1). In that case, ballistic launch angles would have been higher. We derive from published data[44] that they would have been $51.3 \pm 6.5°$ and $46.0 \pm 6.9°$ for Vallis Schrödinger and Vallis Planck, respectively.

The minimum kinetic energy necessary to produce measured craters along Vallis Schrödinger is 1.68×10^{20} J. Because most craters are overlapping, the minimum kinetic energy is likely to be overestimated (~15%) in regions with high secondary crater density. However, gaps between identified craters in other regions offset this effect. Assuming a similar distribution of excavating impacts along the entire crater ray implies a total kinetic energy of 3.39×10^{20} J. Values for Vallis Planck are less well constrained, but higher (~1.21×10^{21} J) because of its greater length. The energy to produce the grand

https://doi.org/10.1038/s41467-024-55675-z

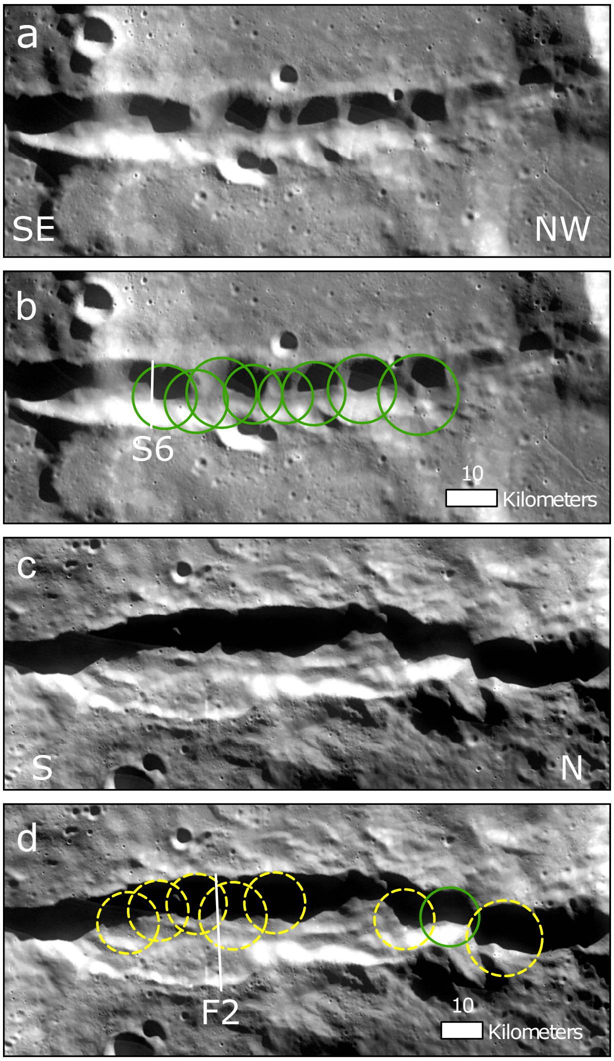

Fig. 3 | Canyon rays. Deepest sections of Vallis Schrödinger (**a** and **b**) and Vallis Planck (**c** and **d**) without and with identified craters. Green circled craters are clearly defined by their eroded crater rims, while yellow circled craters are inferred from the terrain and are not used in the crater scaling calculations. A wall of Valles Planck (lower left of **c** and **d**) appears to have collapsed into the canyon. Location of Supplementary Fig. 6 and Fig. 2 transects are shown (**b** and **d**), respectively.

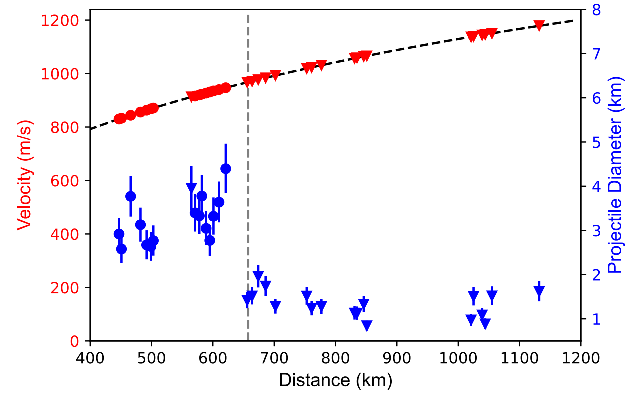

Fig. 4 | Parameters of ballistic flight. Secondary impact velocities (red) and calculated secondary projectile diameters (blue) for Vallis Schrödinger (round symbols) and Vallis Planck (triangular symbols), assuming a 30° flight trajectory, with vertical bars on the symbols representing a range produced by flights from 20 to 45°. Black dashed line is a fit to the secondary impact velocity symbols. The Gray dashed line is the approximate extent of the continuous ejecta blanket.

canyons on the Moon are 1200–2200 times larger than the nuclear explosion energy once planned to excavate a second Panama Canal on Earth, more than 700 times larger than the total yield of US, USSR, and China's nuclear explosion tests, and about 130 times larger than the energy in the global inventory of nuclear weapons[45–48] (Supplementary Table 1).

The extrapolated convergence of Vallis Schrödinger and Vallis Planck suggest a trajectory 33.5° west of north for the asteroid or comet that produced the Schrödinger basin. In contrast, the continuous ejecta blanket covers the greatest distances in a direction 22.3° east of north. We note that direction is downslope, towards the center of the SPA basin. Thus, ejecta may have flowed farther in the downhill direction, towards the SPA basin center, and ejecta blanket extent may not be a measure of the impactor's trajectory. Towards the center of SPA, the edge of the continuous ejecta blanket is ~1 km below the rim of the Schrödinger basin, while the topography rises ~4 km in the opposite direction. Nonetheless, an impactor trajectory 22.3° east of north, as implied by the largest swath of continuous ejecta, rather than 33.5° west of north as implied by the orientation of crater rays, remains possible and is consistent with the rays being lateral sprays of ejecta[44]. In either case, the trajectory of the basin-forming impact is away from the south pole.

Two other asymmetries exist in the Schrödinger basin. A portion of the peak ring is not visible at the surface in one quadrant. That observation was attributed to a preexisting weakness in the crust produced by an older Amundsen-Ganswindt basin-forming impact event[2]. Also, the peak ring rises higher on one side of the basin than on the other, which has been attributed to a change in crustal thickness from 20 to 40 km in the target rocks hit by the Schrödinger impactor[14,19]. Those pre-impact target properties should not, however, have produced two rays that converge near the edge of the Schrödinger basin, rather than its center. An oblique impact away from the south pole must still be the root cause for that convergence. We also note that those peak-ring asymmetries are not aligned with the trajectory of the projectile, implying target properties were more important than trajectory in shaping the peak ring.

Implications for Artemis lunar science

The Schrödinger impact trajectory has important implications for the pending Artemis missions to the south polar region. If ejecta had been distributed symmetrically around the basin, scaling relationships for complex crater ejecta[49] imply 176 $^{+59}_{-44}$ m (at the edge of the Artemis exploration zone) to 42 $^{+29}_{-17}$ m (at the south pole) of ejecta would cover the region. However, a shallow impact trajectory away from the south pole implies highly asymmetric ejecta with a thinner and potentially absent distal ejecta blanket over the Artemis exploration zone. This resolves one of the two greatest uncertainties in estimating the amount of post-SPA debris in the Artemis exploration zone. Still needed is a similar assessment of the distribution of ejecta around the Amundsen-Ganswindt basin which has the potential to cover SPA ejecta, too.

The asymmetric ejecta distribution implied by Schrödinger's crater rays suggests there is less Schrödinger impact ejecta covering candidate landing sites and, thus, astronauts and robotic assets will find it easier to sample SPA and underlying primordial crust samples. Impact craters of order 1 km (similar in size to Arizona's Meteor Crater) can penetrate, excavate, and deposit on the surface material from beneath the Schrödinger impact ejecta blanket. Excavation depth is approximately 1/10 the crater diameter[50], which would be 100–200 m for craters 1–2 km diameter. An impact code parameterized for lunar regolith[51] suggests excavation depths down to 300 m are possible for a 1 km diameter crater. Those values are consistent with the observed excavation and transient crater depths of the 1.25 km Meteor Crater,

which are ~150 m and ~335 m, respectively[52]. Of the 5251 impact craters >1 km in diameter within the Artemis exploration zone, 3243 of them have diameters between 1 and 2 km (ref. 53), indicating access to superposed units (Amundsen-Ganswindt and SPA ejecta) may be common.

The Schrödinger impact basin is the second youngest basin on the lunar surface, so samples of impact melt could be used to test its estimated $3.81^{+0.013}_{-0.014}$ Ga age (ref. 24) and, thus, test the lunar impact cataclysm hypothesis, which posits an enhanced period of impact bombardment at that time[54]; this is the highest priority objective of the National Research Council[3]. Samples from the underlying SPA impact ejecta blanket will provide samples of SPA impact melt, from which the age of the oldest and largest basin on the Moon can be determined. SPA excavated the entire crustal column and upper mantle[55], so a cross-section of the Moon to a depth of ~100 km may be accessible, albeit dismembered. Where craters puncture the SPA ejecta blanket, they can expose primordial crust. Excavated SPA material and any primordial crust can be used to test the lunar magma ocean hypothesis for planetary differentiation and the giant impact hypothesis for the origin of the Earth-Moon system, among many other objectives. Because the Schrödinger impact event dispersed the bulk of its ejecta away from Artemis candidate landing sites, those objectives are more likely to be met.

Terrestrial vs lunar canyon carving processes

The well-preserved Schrödinger basin crater rays provided an opportunity to calculate the velocity of secondary impactors (0.95 to 1.28 km/s), the size distribution of those impactors (up to 5.2 km diameter), and kinetic energy that excavated the resulting canyons (3.39×10^{20} J for Vallis Schrödinger and 1.21×10^{21} J for Vallis Planck). The orientations of the rays imply a primary impact bearing of 33.5° west of north and an impact angle <45° if they formed from downrange ejecta or, alternatively, a bearing of 22.3° east of north if they formed from lateral ejecta. Whereas Arizona's Grand Canyon was carved by water over the last 5 to 6 million years and from integrated paleocanyons that formed over 70 million years[56,57], the Moon's Vallis Schrödinger and Vallis Planck were carved by streams of impacting rock in less than 10 min.

Methods

Spacecraft data analysis

Spacecraft images and elevation data were derived from NASA's Lunar Reconnaissance Orbiter. Data were accessed through the Data Node for Lunar Reconnaissance Orbiter Camera (LROC) Planetary Data System (PDS) products using its Geographic Information System (GIS) QuickMap tool[58], which integrates LROC images with Lunar Orbiter Laser Altimeter (LOLA) elevation data. We used Wide-Angle Camera (WAC) images (100 m/px); narrow-angle camera (NAC) images (0.5 to 2 m/px); NAC region of interest (ROI) mosaics in the Lunar Globe (3D) view; and terrain elevation and slope derived from the LOLA (version SLDEM2015 (+LOLA)) (ref. 59). Secondary craters were identified photogeologically and topographically. QuickMap arc and elevation transect tools were used to measure rim-to-rim diameters of secondary craters in ejecta rays. Three rim-to-rim measurements were taken (i) along the crater ray, (ii) approximately perpendicular to the ray, and (iii) another location where the crater rim was well defined. If the crater rims were ambiguous or the crater seemed heavily modified, a fourth, additional measurement was taken. Possible craters without clearly defined crater rims, too heavily modified craters or craters that are more likely to have been caused by a separate (later) event were disregarded. Some craters in Vallis Planck are marked as "inferred" craters. These likely craters are included in the figures but were not used for any crater scaling or energy calculations. Based on the rim-to-rim diameters, the craters were then (manually) approximated first with a polygon and then with a circle. The final diameter measurement used in subsequent calculations is the diameter of the circle. We compared the average of the three rim-to-rim diameter measurements with the circle diameter. For most craters in Vallis Schrödinger this "error" is less than 5%. It is slightly higher in Vallis Planck due to canyon wall modifications affecting the rim-to-rim diameter measurements. Depth measurements were taken along the profile lines used for the rim-to-rim diameter measurements. Along each of those profile lines, the elevation of the crater rims and the lowest point was determined. The depth was then calculated as $(rim\_1 + rim\_2)/2 - low$. For each crater the maximum depth out of those three or four profiles was then selected. The SLDEM has a typical vertical accuracy of ~3 to 4 m which is sufficient for the depth measurements. For each secondary crater, measurements were made of the distance from the Schrödinger basin center, the intersection point with an inferred transient crater rim[14] on that trajectory, the intersection point of the two largest crater rays (Fig. 1), and the intersection point with the transient crater rim on this trajectory. The procedure accounts for all possible ejection points and, therefore, can be used to estimate minimum to maximum secondary ejecta velocities. For visualization of the results we used ArcMap (v. 10.5.1) and ArcGIS Pro.

Ballistic flight calculations

The crater rays present a unique opportunity to calculate impact velocity (ν) using measured distances between the secondary craters and their ejection point in a ballistic formula for a curved planetary surface:

$$\nu = \left(\frac{gR_p \tan\Phi}{\sin\theta\cos\theta + \cos^2\theta\tan\Phi}\right)^{1/2} \tag{1}$$

where $\Phi = R/2R_p$. We considered ejection and secondary impact angles (Θ) of 20°, 30°, and 45° to account for uncertainty in primary impact angle and ejecta launch position.

Impact scaling calculations

Calculated secondary impact velocities and the diameters of each crater were then used with an analytical scaling relationship for dry sand[60,61] assuming anorthositic norite material[8] with a density of 2,660 kg/m^3 (ref. 62) and a gravity-dominated impact regime, to determine the sizes of impactors and kinetic energy that produced the secondary craters. The secondary craters that produced the canyons are several hundred kilometers away and were formed by impacts at speeds close to 1 km/s. This speed is only just below the speed range of the impact experiments that have been used to develop the crater scaling relationships that we apply in this work[60]. These scaling laws have been shown to be appropriate for some conditions at even lower impact speeds[43,63–66].

Data availability

All data associated with this study are shown in figures and provided in Supplementary Information.

References

1. Kring, D. A. & Durda, D. D. (eds) *A Global Lunar Landing Site Study to Provide the Scientific Context for Exploration of the Moon* (Lunar and Planetary Institute, Houston, 2012).
2. Shoemaker, E. M., Robinson, M. S. & Eliason, E. M. The south pole region of the moon as seen by Clementine. *Science* **266**, 1851–1854 (1994).
3. National Resource Council, *The Scientific Context for Exploration of the Moon* (The National Academies Press, Washington D. C., 2007).
4. Mest, S. C. in Recent Advances in Lunar Stratigraphy 477 (eds Williams, D. A.& Ambrose, W.) 95–115 (Geological Society of America Special Paper, 2011).

5. O'Sullivan, K. M., Kohout, T., Thaisen, K. G.& Kring, D. A. in Recent Advances in Lunar Stratigraphy 477 (eds Williams, D. A.& Ambrose, W.) 117–138 (Geological Society of America Special Paper, 2011).
6. Bunte, M. K., Porter, S. & Robinson, M. S. in *Analogs for Planetary Exploration* 483 (eds Garry, W. B. & Bleacher, J. E.) 533–546 (Geological Society of America, 2011).
7. Shankar, B., Osinski, G. R., Antonenko, I. & Neish, C. D. A multispectral geological study of the Schrödinger impact basin. *Can. J. Earth Sci.* **50**, 44–63 (2013).
8. Kramer, G. Y., Kring, D. A., Nahm, A. L. & Pieters, C. M. Spectral and photogeologic mapping of Schrödinger basin and implications for post-South Pole-Aitken impact deep subsurface stratigraphy. *Icarus* **223**, 131–148 (2013).
9. Kumar, P. S. et al. Gullies and landslides on the moon: evidence for dry-granular flows. *J. Geophys. Res. Planets* **118**, 1–18 (2013).
10. Klimczak, C. Geomorphology of lunar grabens requires igneous dikes at depth. *Geology* **42**, 963–966 (2014).
11. Hurwitz, D. & Kring, D. A. Potential sample sites for South Pole-Aitken basin impact melt within the Schrödinger basin. *Earth Planet. Sci. Lett.* **427**, 31–36 (2015).
12. Potts, N. J. et al. Robotic traverse and sample return strategies for a lunar farside mission to the Schrödinger basin. *Adv. Space Res.* **55**, 1241–1254 (2015).
13. Kumar, P. S., et al. Recent shallow moonquake and impact-triggered boulder falls on the moon: new insights from the Schrödinger basin. *J. Geophys. Res. Planets* **121**, 147–179 (2016).
14. Kring, D. A., Kramer, G. Y., Collins, G. S., Potter, R. W. K. & Chandnani, M. Peak-ring structure and kinematics from a multi-disciplinary study of the Schrödinger impact basin. *Nat. Commun.* **7**, 13161 (2016).
15. Steenstra, E. S. et al. Analyses of robotic traverses and sample Sites in the Schrödinger basin for the HERACLES human-assisted sample return mission concept. *Adv. Space Res.* **58**, 1050–1065 (2016).
16. Allender, E. J. et al. Traverses for the ISECG-GER design reference mission for humans on the lunar surface. *Adv. Space Res.* **63**, 692–727 (2019).
17. Czaplinski, E. C. et al. Human-assisted sample return mission at the Schrödinger basin, lunar farside using a new geologic map and rover traverses. *Planet. Sci. J.* **2**, 51 (2021).
18. Kring, D. A. et al. Prominent volcanic source of volatiles in the south polar region of the moon. *Adv. Space Res.* **68**, 4691–4701 (2021).
19. Kring, D. A. et al. Chicxulub and the exploration of large peak-ring impact craters through scientific drilling. *GSA Today* **27**, 4–8 (2017).
20. Alvarez, L. W., Alvarez, W., Asaro, F. & Michel, H. V. Extraterrestrial cause for the Cretaceous–Tertiary extinction. *Science* **208**, 1095–1108 (1980).
21. Smit, J. & Hertogen, J. An extraterrestrial event at the Cretaceous–Tertiary boundary. *Nature* **285**, 198–200 (1980).
22. Hildebrand, A. R. et al. The Chicxulub crater: a possible cretaceous-tertiary boundary impact crater on the Yucatán Peninsula, Mexico. *Geology* **19**, 867–871 (1991).
23. Kring, D. A. & Boynton, W. V. The petrogenesis of an augite-bearing melt rock in the Chicxulub structure and its relationship to K/T impact spherules in Haiti. *Nature* **358**, 141–144 (1992).
24. van der Bogert, C. H., Poehler, C. M., Kring, D. A. & Hiesinger, H. Absolute model ages for geological units in Schrödinger basin: Context for the 2024 PRISM CLPS mission. *Lunar Planet. Sci. LII*, 2351 (2021).
25. Nesvorný, D. et al. Early bombardment of the moon: connecting the lunar crater record to the terrestrial planet formation. *Icarus* **399**, 115545 (2023).
26. Garrick-Bethell, I. & Zuber, M. T. Elliptical structure of the lunar South Pole-Aitken basin. *Icarus* **204**, 399–408 (2009).
27. Fortezzo, C. M., Spudis, P. D. & Harrell, S. L. *Unified Geologic Map of the Moon, 1:5M* (United States Geological Survey, Flagstaff, 2020).
28. Wilhelms, D., Howard, K., & Wilshire, H. *Geological Map of the South Side of the Moon: Miscellaneous Investigations Map I-1162* (United States Geological Survey, Flagstaff, 1979).
29. Allen, C. C. Large lunar secondary craters—Size-range relationships. *Geophys. Res. Lett.* **6**, 51–54 (1979).
30. Pike, R. J. Geometric interpretation of lunar craters, *U.S. Geological Survey Profesional Paper 1046-C*, 1–77 (1980).
31. Stopar, J. D. et al. Relative depths of simple craters and the nature of the lunar regolith. *Icarus* **298**, 34–48 (2017).
32. Pike, R. J.& Wilhelms, D. E. Secondary-impact craters on the moon: Topographic form and geologic process. *Lunar Planet. Sci.* **IX**, 907–909 (1978).
33. Bickel, V. T. et al. Analysis of lunar boulder tracks: implications for trafficability of pyroclastic deposits. *J. Geophys. Res. Planets* **124**, 1296–1314 (2019).
34. Melosh, H. J. Impact ejection, spallation, and the origin of meteorites. *Icarus* **59**, 234–260 (1984).
35. Lucchitta, B. K. Crater clusters and light mantle at the Apollo 17 site: a result of secondary impact from Tycho. *Icarus* **30**, 80–96 (1977).
36. Schultz, P. H. & Gault, D. E. Clustered impacts: experiments and implications. *J. Geophys. Res.* **90**, 3701–3732 (1985).
37. Singer, K. N., Jolliff, B. L. & McKinnon, W. K. Lunar secondary craters and estimated ejecta block sizes reveal a scale-dependent fragmentation trend. *J. Geophys. Res. Planets* **125**, e2019JE006313 (2020).
38. Schultz, P. H. & Crawford, D. A. Lunar basin-forming projectiles. *Lunar Planet. Sci. LXV*, 1961 (2014).
39. Kring, D. A. *Guidebook to the Geology of Barringer Meteorite Crater, Arizona (a.k.a. Meteor Crater)* (Lunar and Planetary Institute, Houston, 2017).
40. Guo, D., Liu, J. & Head, J. W. III Lunar Orientale impact basin secondary craters: spatial distribution, size-frequency distribution, and estimation of fragment size. *J. Geophys. Res.* **123**, 1344–1367 (2018).
41. Anderson, J. L. B., Schultz, P. H. & Heineck, J. T. Asymmetry of ejecta flow during oblique impacts using three-dimensional particle image velocimetry. *J. Geophys. Res.* **108**, E8 (2003).
42. Schultz, P. & Crawford, D. Origin and implications of non-radial Imbrium sculpture on the moon. *Nature* **535**, 391–394 (2016).
43. Gault, D. E. & Wedekind, J. A. experimental studies of oblique impact. *Proc. 9th Lunar Planet. Sci. Conf.*, 3843–3875 (1978).
44. Luo, X.-Z., Zhu, M.-H. & Ding, M. Ejecta patterns of oblique impacts on the moon from numerical simulations. *J. Geophys. Res. Planets* **127**, e2022JE007333 (2022).
45. New York Times, A new canal - dug by atom bombs; nuclear energy is the key to replacing our obsolescent big ditch with a bigger one (September 20, 1964).
46. Andryshin, I. A. et al. *USSR Nuclear Weapons Tests and Peaceful Nuclear Explosions, 1949 through 1990* (RFNC-VNIIEF, Sarov, 1996).
47. Department of Energy, United States Nuclear Tests, July 1945 through September 1992, DOE/NV-209-REV16 (United States Government, Washington, D. C., 2015).
48. Mizokami, K. et al. *What If We Blew Up All the World's Nukes at Once? Popular Mechanics* (April 22, 2022).
49. Kring, D. A. The dimensions of the Chicxulub impact crater and impact melt sheet. *J. Geophys. Res.* **100**, 16,979–16,986 (1995).
50. Melosh, H. J. et al. *Impact Cratering: A Geologic Process* (Oxford University Press, New York, 1989).
51. Holsapple, K. A. et al. (downloaded and utilized 1/2023) Code was made publicly available through the website https://www.lpi.usra.edu/lunar/tools/lunarcratercalc/.
52. Roddy, D. J., Boyce, J. M., Colton, G. W. & Dial. A. L. Jr. Meteor Crater, Arizona, rim drilling and thickness, structural uplift, diameter, depth, volume, and mass-balance calculations. *Proc. 6th Lunar Science Conf.*, 2621–2644 (1975).

53. Früh, T., *et al Topographic Map and >1 km-diameter Craters in the Artemis Exploration Zone, Lunar South Pole Atlas* (Lunar and Planetary Institute, Houston, 2023).
54. Tera, F., Papanastassiou, D. A. & Wasserburg, G. J. Isotopic evidence for a terminal lunar cataclysm. *Earth Planet. Sci. Lett.* **22**, 1–21 (1974).
55. Potter, R. W. K., Collins, G. S., Kiefer, W. S., McGovern, P. J. & Kring, D. A. Constraining the size of the South Pole-Aitken basin impact. *Icarus* **220**, 730–743 (2012).
56. Flowers, R. M. & Farley, K. A. Apatite $^{4}He/^{3}He$ and (U-Th)/He evidence for an ancient Grand Canyon. *Science* **338**, 1616–1619 (2012).
57. Karlstrom, K. E. et al. Formation of the grand canyon 5 to 6 million years ago through integration of older paleocanyons. *Nat. Geosci.* **7**, 239–244 (2014).
58. Bowman-Cisneros, E., et al. Enhanced lunar reconnaissance orbiter camera planetary data system data node. *Lunar Planet. Sci.* ***XLV***, 2584 (2014).
59. Barker, M. K. et al. A new lunar digital elevation model from the Lunar Orbiter Laser Altimeter and SELENE Terrain Camera. *Icarus* **273**, 346–355 (2016).
60. Schmidt, R. M. & Housen, K. R. Some recent advances in the scaling of impact and explosion cratering. *Intern. J. Impact Eng.* **5**, 543–560 (1987).
61. Holsapple, K. A. The scaling of impact processes in planetary sciences. *Ann. Rev. Earth Planet. Sci.* **21**, 333–373 (1993).
62. Kiefer, W. S., Macke, R. J., Britt, D. T., Irving, A. J. & Consolmagno, G. J. The density and porosity of lunar rocks. *Geophys. Res. Lett.* **39**, L07201 (2012).
63. Hartmann, W. K. Impact experiments 1: ejecta velocity distributions and related results from regolith targets. *Icarus* **63**, 69–98 (1985).
64. Holsapple, K. A. & Schmidt, R. M. On the scaling of crater dimensions: 1. Impact processes. *J. Geophys. Res.* **87**, 1849–1870 (1982).
65. Ormö, J. et al. Scaling and reproducibility of craters produced at the Experimental Projectile Impact Chamber (EPIC), Centro de Astrobiología, Spain. *Meteorit. Planet. Sci.* **50**, 2067–2086 (2015).
66. Yamamoto, S., Hasegawa, S., Suzuki, A. I. & Matsunaga, T. Impact velocity dependence of transient crater growth. *J. Geophys. Res. Planets* **122**, 1077–1089 (2017).

Acknowledgements
Research supported by NASA Solar System Exploration Research Virtual Institute contract 80NSSC20M0016 (DAK), NASA's Lunar and Planetary Institute cooperative agreement with the Universities Space Research Association (DAK, DPK), and UK Science and Technology Facilities Council Grant ST/S000615/1 (DPK, GSC). LPI Contribution No. 3086.

Author contributions
D.A.K. conceived the project. D.P.K. and D.A.K. conducted the photogeologic study and D.P.K., D.A.K., and G.S.C. implemented impact cratering calculations. All authors contributed to writing and editing the manuscript.

Competing interests
The authors declare no competing interests.

Additional information
Supplementary information The online version contains supplementary material available at https://doi.org/10.1038/s41467-024-55675-z.

Correspondence and requests for materials should be addressed to David A. Kring.

Peer review information *Nature Communications* thanks the anonymous reviewers for their contribution to the peer review of this work. A peer review file is available.